





Actin-ring segment switching drives nonadhesive gap closure

Qiong Wei^{a,1}, Xuechen Shi^{b,1}, Tiankai Zhao^a, Pingqiang Cai^c, Tianwu Chen^a, Yao Zhang^a , Changjin Huang^d , Jian Yang^b , Xiaodong Chen^c, and Sulin Zhang^{a,b,2}

^aDepartment of Engineering Science and Mechanics, Pennsylvania State University, University Park, PA 16802; ^bDepartment of Biomedical Engineering, Pennsylvania State University, University Park, PA 16802; ^cDepartment of Materials Science and Engineering, Nanyang Technological University, 639798 Singapore, Singapore; and ^dDepartment of Mechanical and Aerospace Engineering, Nanyang Technological University, 639798 Singapore, Singapore

Edited by Philip LeDuc, Carnegie Mellon University, Pittsburgh, PA, and accepted by Editorial Board Member John A. Rogers November 6, 2020 (received for review June 7, 2020)

Gap closure to eliminate physical discontinuities and restore tissue integrity is a fundamental process in normal development and repair of damaged tissues and organs. Here, we demonstrate a nonadhesive gap closure model in which collective cell migration, large-scale actin-network fusion, and purse-string contraction orchestrate to restore the gap. Proliferative pressure drives migrating cells to attach onto the gap front at which a pluricellular actin ring is already assembled. An actin-ring segment switching process then occurs by fusion of actin fibers from the newly attached cells into the actin cable and defusion from the previously lined cells, thereby narrowing the gap. Such actin-cable segment switching occurs favorably at high curvature edges of the gap, yielding size-dependent gap closure. Cellular force microscopies evidence that a persistent rise in the radial component of inward traction force signifies successful actin-cable segment switching. A kinetic model that integrates cell proliferation, actin fiber fusion, and purse-string contraction is formulated to quantitatively account for the gap-closure dynamics. Our data reveal a previously unexplored mechanism in which cells exploit multifaceted strategies in a highly cooperative manner to close nonadhesive gaps.

gap closure | actin ring | traction force microscopy | cell patterning

Closure of open gaps and wounds in tissues and organs is a morphogenetic process essential to both normal development and tissue repair (1). A critical step of gap closure involves collective cell migration to restore the mechanical integrity of the tissues, regain the barrier function, and recover tissue homeostasis (1–5). Two distinct mechanisms have been identified to account for epithelial gap closure and wound healing (6, 7). Across an adhesive gap, cells at the wound border migrate into the wound area by extending protrusive lamellipodia (8, 9), featuring a cell-crawling mechanism. Across nonadhesive or severely damaged gaps (10, 11), cells assemble a supracellular actin ring that lines around the gap (12–16), resembling a purse string. Such a supracellular actin cable senses and responds to the local curvature of the gap (17, 18), contracting and pulling the follower cells, thus enabling cell bridging over the nonadhesive gaps and gap closure, the biomechanical basis for nonadhesive gap closure has remained not fully understood.

From a biomechanics point of view, the contraction of an actin ring of radius R scales with $\kappa\gamma$, where $\kappa = 1/R$ is the curvature of the actin ring, and γ is its contractility (force per unit length), which is generally limited by the contractile machinery of the cells. This suggests that the purse-string contraction mechanism has a gap-size limit beyond which the contraction $\kappa\gamma$ is not powerful enough to close the gap. Such size-limiting gap-closure phenomena have been previously reported (16, 19), and the failure of gap closure is often accompanied by a three-dimensional (3D) pileup of cells at the adherent/nonadherent wound interface (16, 19, 20). Here, we show that Madin-Darby Canine Kidney (MDCK) cells fight against the size limit by

exploiting coordinated cell proliferation, collective cell migration, actin-network reorganization, and purse-string contraction. The cell proliferative pressure pushes migrating cells to attach onto the gap front, triggering actin-ring segment switching by fusion of actin fibers from the newly attached cells into the actin ring and defusion from the previously lined cells. Such a switching process effectively advances the gap front and subsequently empowers the actin-ring contraction (by increasing κ). We further rationalize that such actin-ring segment switching is local-curvature dependent, thereby revealing a different size dependence in gap closure from the classical purse-string contraction mechanism. By integrating purse-string contraction and cell proliferation, we formulate a kinetic model to account for the gap closure dynamics. Taken together, our study unveils that cell proliferation and migration, actin-cytoskeleton remodeling, and cellular force generation and transmission are coordinated in space and synchronized in time to drive epithelial closure of nonadhesive gaps.

Curvature-Dependent Nonadhesive Gap Closure

Using the deep-UV-based micropattern technique (21) with modifications, type-I collagens were conjugated to specific

Significance

Gap closure to eliminate physical discontinuities and restore tissue integrity is a fundamental process in normal development and repair of damaged tissues and organs. Here, we report a previously unexplored gap-closure mechanism by which cell proliferation, collective cell migration, large-scale intercellular actin-network remodeling, and purse-string contraction act in a highly coordinated manner to restore the gap. In distinct contrast to the classical purse-string contraction mechanism, this mechanism involves intercellular switching of actin-cable segments at the gap front, which effectively empowers the actin cable for gap closure. Our study highlights the principles of wound healing driven by the close reciprocity between mechanics and cellular remodeling and might inspire mechanobiological intervention strategies for embryogenesis, tissue repair, antimetastasis, and plastic surgery.

Author contributions: Q.W., X.S., C.H., and S.Z. designed research; Q.W., X.S., T.Z., P.C., T.C., and Y.Z. performed research; Q.W., X.S., T.Z., P.C., J.Y., X.C., and S.Z. contributed new reagents/analytic tools; Q.W., X.S., T.Z., P.C., and S.Z. analyzed data; and Q.W., X.S., and S.Z. wrote the paper.

The authors declare no competing interest.

This article is a PNAS Direct Submission. P.L. is a guest editor invited by the Editorial Board.

Published under the PNAS license.

¹Q.W. and X.S. contributed equally to this work.

²To whom correspondence may be addressed. Email: suz10@psu.edu.

This article contains supporting information online at <https://www.pnas.org/lookup/suppl/doi:10.1073/pnas.2010960117/-DCSupplemental>.

regions of polyacrylamide (PAA) hydrogels with physiologically relevant elasticity, forming arrays of adhesive patterns of different sizes and shapes (see *Materials and Methods*). Alternatively, microcontact printing can be applied to prepare adhesive patterns (see *Materials and Methods*). After being seeded onto the hydrogels, MDCK cells adhered to the collagen-coated surface and proliferated and spread to cover the entire adhesive domains in about 40 h, forming cell monolayers of well-defined size and shape with a gap at the center devoid of adhesive molecules (Fig. 1A). The closure process was then monitored for another 2 to 3 d. At day 5, the MDCK monolayers had a significantly high probability (~ 1.0) to bridge over the circular gaps with a radius of 50 μm , a relatively low probability (< 0.5) to bridge over elliptical gaps with equivalent radii ($R_{eq} = \sqrt{A/\pi}$) of 61.2 μm (major/minor radii, 75/50 μm) and 70.7 μm (major/minor radii, 100/50 μm), respectively, and zero probability to bridge over the circular gaps of 100 μm in radius (Fig. 1B). After day 5 of culture, the closure probabilities of all of the gaps remained nearly unchanged for further prolonged culture, which was consistent with a previous study (19). Since the circular gaps with 100 μm in radius showed negligible change in size over 5 d of culture, it was unlikely the gap could ever close for further prolonged culture time. This closure probability was, however, nearly independent on the overall size and shape of the MDCK monolayers (Fig. 1B). Although it is challenging to determine the size thresholds of gaps owing to the statistical nature, our experiments identified a rough size range: below 50 μm in radius, nearly all of the circular gaps can successfully close, and beyond 100 μm in radius, all of the circular gaps cannot. We further observed that closure of the elliptical gaps always started from the high-curvature regions, that is, along the long axis (*SI Appendix, Fig. S1*). As such, an elliptical-to-circular shape transition occurred for the elliptical gaps at the initial stage of gap closure, after which the gap-closure process resembled that of the circular gaps. Taken together, our experimental data show that closure of nonadhesive gaps is curvature dependent and high curvature favors gap closure.

To capture the closure dynamics, the perimeter of the gap was tracked over time (Fig. 1C). For all of the cases, the starting point of tracking was set to be the time when the cells became confluent in the adhesive domains, about 40 h after seeding the

cells on the hydrogels. The gap-closure rate was generally non-linear with time. For the 50- μm circular gaps, gap closure exhibited a relatively slow kinetics at the initial stage (0 to 5 h after closure began), followed by a relatively fast bridging regime. For the 100 μm circular gap, the gap perimeter slightly decreased at the initial stage (0 to 5 h), after which the perimeter stayed nearly unchanged over time, showing the gap closure was halted. Closure of the elliptical gaps manifested three regimes: an initial regime at which the perimeter of the elliptical gaps decreased rapidly (0 to 5 h), corresponding to the invasion of the high-curvature regions; a second regime at which the closure was nearly halted (5 to 20 h), corresponding the transition from elliptical to circular-shaped gaps; and a third regime with closure kinetics similar to that of the circular gaps.

Both Purse-String Contraction and Cell Proliferation Contributed to Nonadhesive Gap Closure

We tracked the nonadhesive gap closure process by immunofluorescence staining of F-actins at different time points. For all of the gaps, a pluricellular actin ring formed, lining the cells at the gap front. The closure over the 50- μm nonadhesive gaps took ~ 30 to 50 h, nearly 10-times longer than that over adhesive gaps of comparable size for which cell crawling drives the closure (22). No lamellipodia similar to those in adhesive wound were observed. The 3D confocal images evidenced that bridging cells attached to the gap front, suspending over but without adhering to the bare hydrogel surface (Figs. 2A and 3A). These observations suggested that the closure of the nonadhesive gaps was not driven by lamellipodial protrusion-based cell crawling at the wound border. Previous experiments have shown that Laminin-5 plays an important role in MDCK migration in scratch or laser-ablation assays or when cell layers are subconfluent (23–25). In our nonadhesive gap model, the MDCK cell layers were naturally grown without introducing any physical damages, and the cells became confluent before invading the nonadhesive gaps. Thus, it is unlikely that Laminin-5 plays the similarly important role in our gap-closure model. We then asked whether the purse-string contraction mechanism was active for the MDCK cells. We treated the cells with blebbistatin to inhibit actomyosin II contraction and found that blebbistatin treatment markedly reduced the gap-closure probability (Fig. 2B and C), suggesting

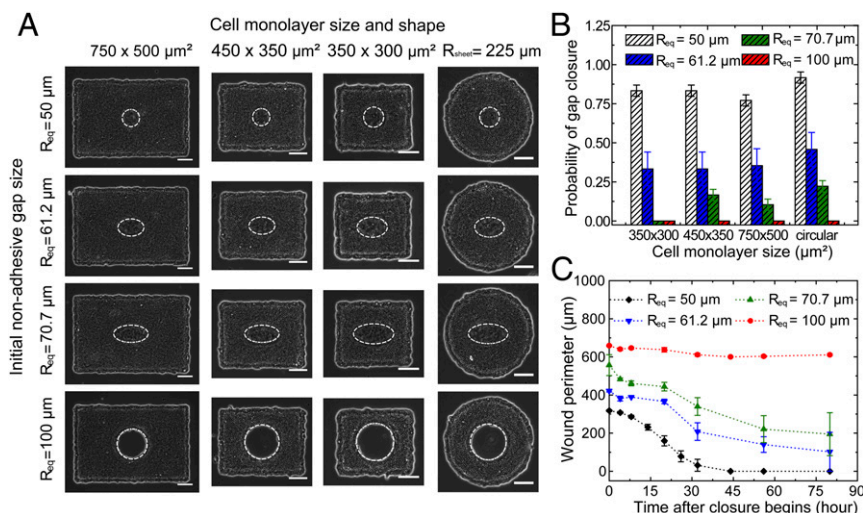


Fig. 1. Gap-size-dependent closure of the MDCK cell monolayers over nonadhesive gaps. (A) Representative gap-closure behaviors at day 5 of culture for different initial gap sizes (denoted by the white dashed lines, elliptical gaps: major/minor radii, 75/50 μm for $R_{eq} = 61.2 \mu\text{m}$, and 100/50 μm for $R_{eq} = 70.7 \mu\text{m}$, respectively) and different monolayer sizes on 6 kPa hydrogel. Scale bar, 100 μm . (B) Closure probability for different gap sizes and different monolayer sizes. For each gap type, data were collected from $n = 48$ gaps. (C) Gap closure kinetics (starting at 40 h after cell seeding). The sample size ranges from 5 (for $R_{eq} = 61.2 \mu\text{m}$ and $R_{eq} = 70.7 \mu\text{m}$ gaps) to 13 (for $R = 50$ and 100 μm gaps) at each time point for different initial gap sizes.

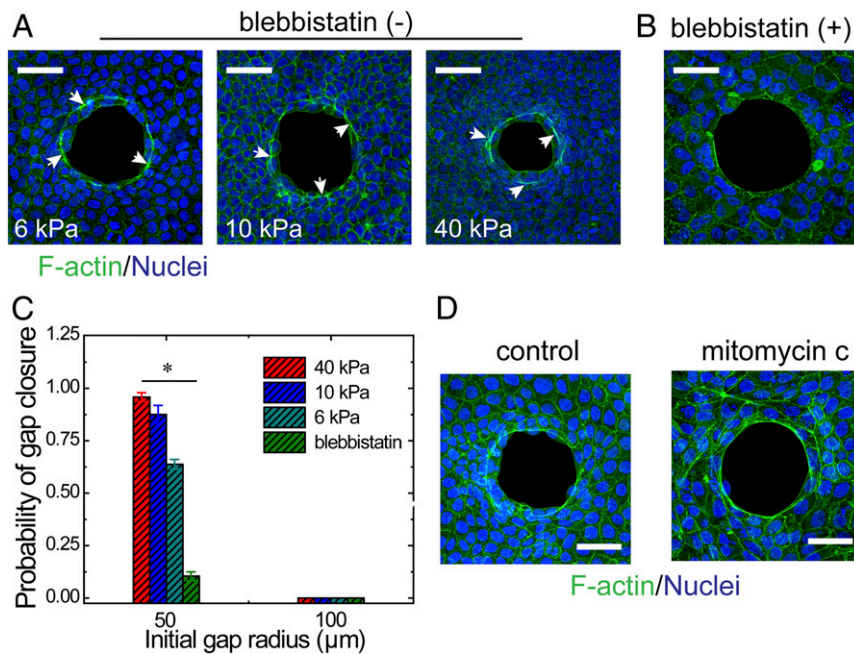


Fig. 2. The influence of cell contractility and cell proliferation on the nonadhesive gap closure. (A) With increasing gel stiffness, cell contractility increases, and so does the gap-closure probability. The white arrows point to the actin ring segments. (B) Blebbistatin inhibits cell contractility and hence the actin-ring formation, leading to decreased gap-closure probability. (C) Cell contractility and substrate stiffness-dependent gap-closure probability at day 4 of culture. Increasing hydrogel stiffness increases the closure probability of the 50- μm -radius gaps at day 4 of culture but has negligible effects on the closure probability at day 5 of culture, beyond which the closure probability of the gaps remains nearly unchanged. Sample size: $n = 48$ gaps. $*P < 0.05$. (D) Adding mitomycin C inhibits cell proliferation and cell attachment to the gap front, but the formation of the actin ring at the gap edge is nearly unaffected. The white arrows point to cells attached onto the gap front in the absence of mitomycin C. Scale bar, 50 μm .

that purse-string contraction contributed to the nonadhesive gap closure. Since a small fraction of gaps still closed under inhibited cell contractility, other mechanisms may be active in the gap-closure process.

Adherent cells sense extracellular matrix (ECM) stiffness and respond by increasing cell contractility (26) and proliferation (27). We then tuned the stiffness of the hydrogels by altering the cross-linking level to infer whether hydrogel stiffness would influence the closure process of the nonadhesive gaps. We compared the closure probabilities of the circular gaps with a 50- μm radius at day 4 and day 5 of culture. We found that at day 4 of culture, the closure probabilities increased with increasing hydrogel stiffness (Fig. 2C), whereas at day 5 of culture, the closure probabilities of the 50- μm -radius gaps were nearly the same, regardless of the hydrogel stiffness (and further continued culture caused little changes in the close probability). For the 100- μm circular gaps, the closure probabilities for all of the gaps remained nearly zero both at day 4 and day 5 of culture, regardless of the hydrogel stiffness. These comparative data suggest that increasing hydrogel stiffness has a strong effect on how fast a gap can close but little effect on whether or not the gap can eventually close. We further observed that a stiff hydrogel did not cause an obvious change in the thickness of the pluricellular actin ring as indicated by immunofluorescence staining of F-actins (Fig. 2A), although this cannot completely preclude the possibility that increasing hydrogel stiffness may increase the actin-ring contraction. Taken together, increasing hydrogel stiffness markedly increases the closure kinetics for gaps that can close but insignificantly affects the overall closure probability of the gaps for sufficiently long culture time.

We further explored the role of cell proliferation in the closure of a 50- μm nonadhesive gap. We added mitomycin C to inhibit cell proliferation immediately after cells became confluent in adhesive domains and monitored cell movements at the

gap front. Mitomycin C caused cell death for prolonged culture. We thus confined our observations within the next 12 h after mitomycin C was added, a period that the cells still remained active. We found that adding mitomycin C halted the gap-closure process for all of the gaps despite that the pluricellular actin ring still formed (Fig. 2D). In particular, with mitomycin C treatment, cells no longer attached onto the gap front, which was distinctly different from the control experiments observed in the same time period (Fig. 2D), suggesting that successful cell attachment to the gap front was enabled by proliferative pressure (*SI Appendix, Fig. S2*). Collectively, our results show that both purse-string contraction and cell proliferation contributed to the nonadhesive gap closure. This gap-closure mechanism is distinctly different from the classical purse-string contraction whereby cell proliferation negligibly affects the wound-healing process (16, 28).

Closure of Nonadhesive Gaps Involves Actin-Ring Segment Switching

The closure process of the MDCK monolayer over the nonadhesive gaps was accompanied by dynamic evolution of the pluricellular actin ring along the gap edge (Fig. 3A). The actin ring is constituted of segments contributed by a group of cells and linked intercellularly through adherens junctions (13, 29, 30). For all of the gaps, the actin ring started as a continuous cable bordering the gaps, similar to the classical purse-string contraction mechanism (Fig. 3A, 40 h; Fig. 3B, 40 h; Fig. 3C, 48 h). For small nonadhesive gaps, confocal images revealed that consecutive cell attachment and spreading occurred at the gap edge (Fig. 3A, 44 to 60 h). Due to cell attachment onto the gap front, some actin-ring segments were not always at the advancing front of the gap but sometimes located one or two cell layers behind the border (Fig. 3A, 48 to 60 h, *SI Appendix, Fig. S3*), and the maximal lagging distance occurred at around 55 h (*SI Appendix,*

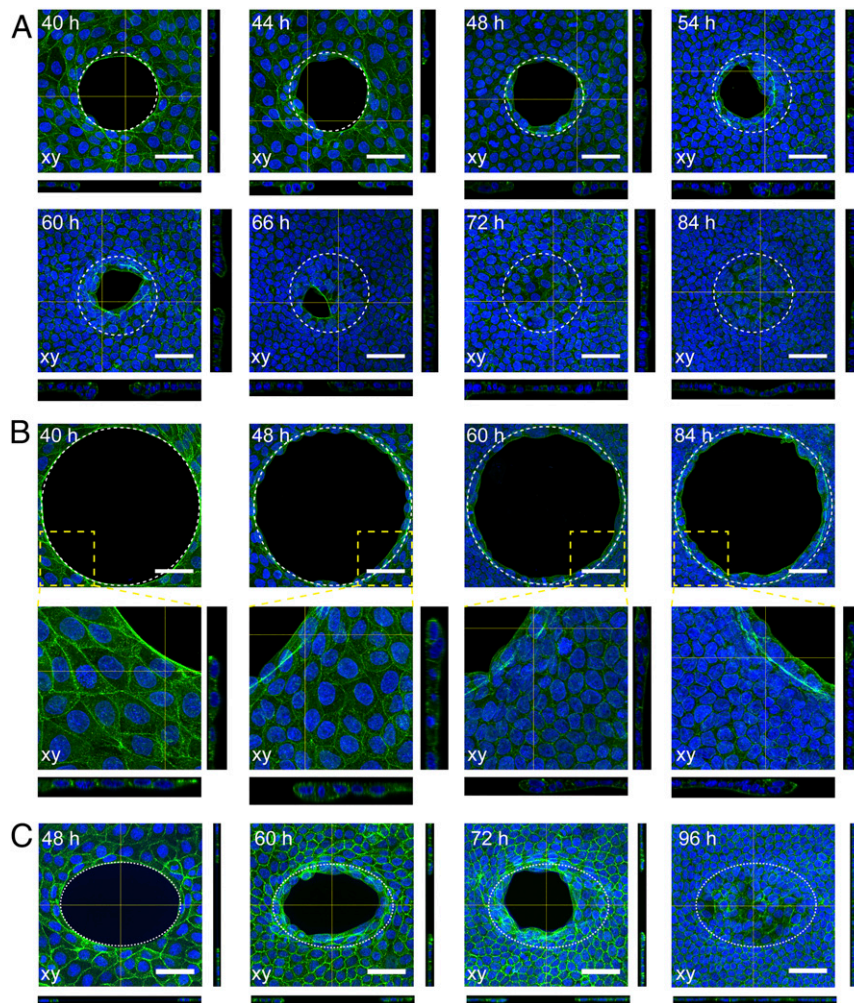


Fig. 3. The time evolution of F-actin and cell morphologies at the gap boundary is determined by the nonadhesive gap size. (A) A circular gap with $R_{eq} = 50 \mu\text{m}$. (B) A circular gap with $R_{eq} = 100 \mu\text{m}$. (C) An elliptical gap with $R_{eq} = 61.2 \mu\text{m}$ (major/minor radii, $75/50 \mu\text{m}$). The white dashed lines indicate the initial gap regions. Scale bar, $50 \mu\text{m}$. Green/blue: F-actin/nuclei.

Fig. S3). As the gap became smaller, some actin-ring segments could reappear at the wound front (Fig. 3A, 66 h). This process continued until a confluent bridging cell monolayer eventually suspended over the entire gap. This is in distinct contrast to the classical purse-string contraction mechanism, where the actin ring always stays at the gap front, preventing individual cells bordering the wound from migrating forward on their own throughout the gap-closure process (2, 16). Recall that inhibition of cell proliferation by the mitomycin C treatment eliminated cell attachment onto the gap front, leaving the actin ring staying always at the gap front (Fig. 2D). This indicated that the change of the positions of the actin-ring segments was due to the proliferation-dependent cell attachment to the gap front.

For large nonadhesive gaps ($100 \mu\text{m}$), similar cell attachment to the gap front was observed (Fig. 3B, 48 to 84 h). However, instead of bridging over the gap, the attached cells piled up at the wound border (Fig. 3B, 84 h), exhibiting an edge-enhancement phenomenon as previously reported (20), which resembles the formation of burls in nature. The pileup of cells for large gaps also resembles the morphology of MDCK cell clusters seeded on soft substrate, where cells spread and form a monolayer on stiff hydrogels but aggregate and form a multilayer on soft hydrogels (SI Appendix, Fig. S4). For small elliptical gaps with an equivalent radius of $61.2 \mu\text{m}$, a pluricellular actin ring also formed at the gap front. Similar repositioning of the actin-ring segments as

seen in $50\text{-}\mu\text{m}$ circular gaps was also observed. Differently, the cells invaded first the high-curvature regions (Fig. 3C, 60 h). The gap closure thus proceeded in such a way that the gap underwent an elliptical-to-circular shape transition (Fig. 3C, 60 to 72 h), after which the gap-closure process resembled that of the $50\text{-}\mu\text{m}$ circular gaps.

To further confirm the actin-ring segment switching process, we performed live-cell imaging of MDCK cells that stably expressed LifeAct-GFP (Green Fluorescent Protein) (Fig. 4A and Movies S1 and S2). Two cells were particularly highlighted in red and blue, showing their position exchange at the gap front. Before the swap, the blue cell contributed its actin segment to the actin ring at the gap front. After the swap, the blue cell was pushed back, and the red cell appeared at the gap front. Concomitant to the swap of the positions of the cells, the actin-ring segment switched (Fig. 4A, Bottom). The dynamic switching of the actin-ring segments supports a previously unreported gap-closure mechanism: as a new cell migrates and attaches onto the gap front, an actin-ring segment assembles within the newly attached cells and is subsequently fused into the actin ring; meanwhile, the actin-ring segment from the previous cells (behind the newly attached cells) disassembles and is defused from the actin cable. This actin-ring segment switching process effectively advances the gap front. The transient characteristics, such as diminishing segments of the actin ring (Fig. 3A, 48 h),

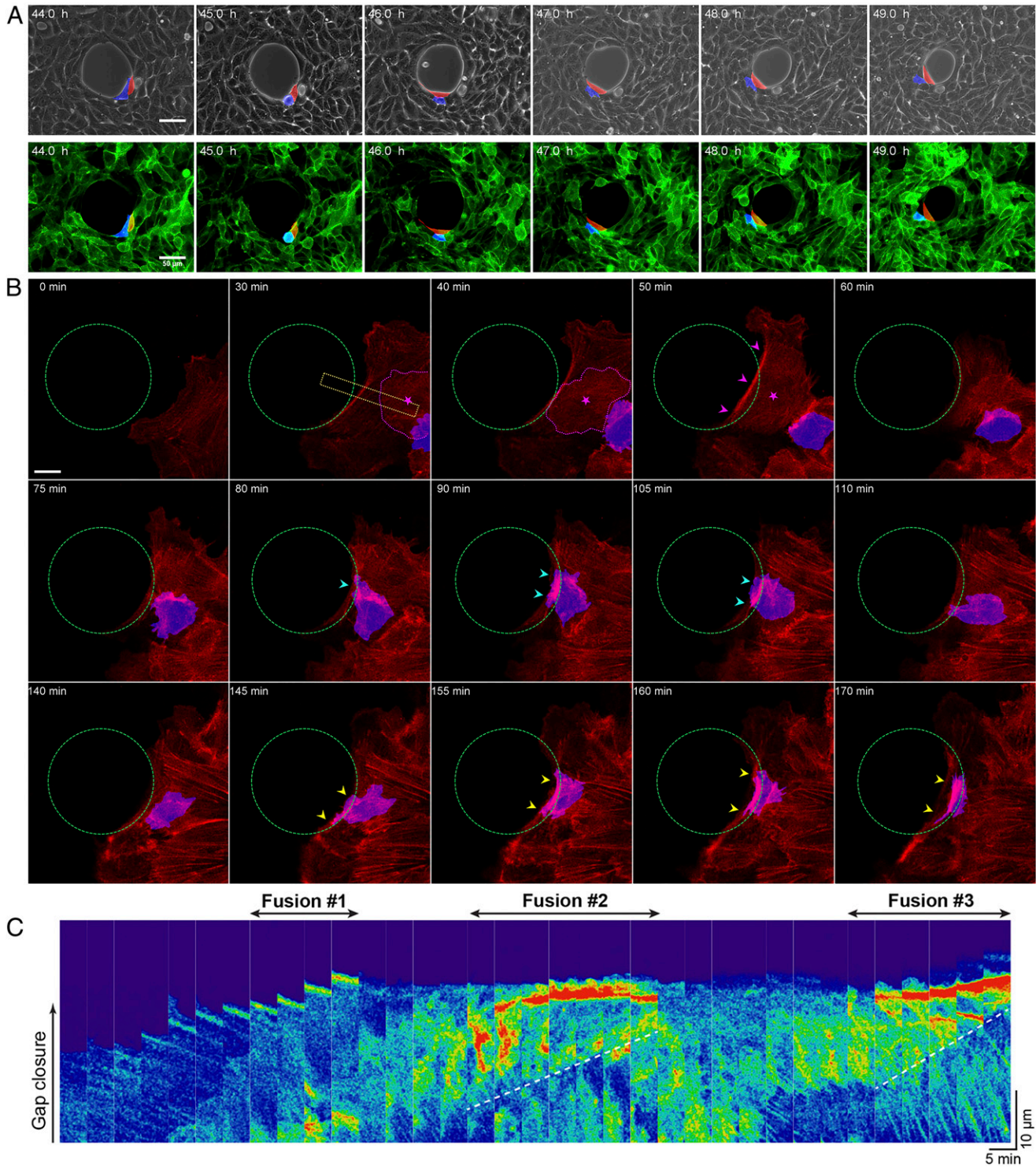


Fig. 4. Live-cell imaging of the gap-closure process. (A, *Top*) Time-lapse phase-contrast images showing the swapping in positions of two MDCK cells at the gap front. (*Bottom*) Time-lapse images using LifeAct-GFP-expressing MDCK cells, showing the updating actin network due to the swap of the cells at the gap front. Initial gap radius: 50 μm . The manually highlighted cells, in red and blue, swapped their locations. Scale bar, 50 μm . (B) Confocal fluorescent imaging of the leading front of MDCK cells tagged with LifeAct-RFP when crossing the nonadhesive gap (dashed green circle; diameter of 40 μm). Three events of one follower cell (denoted with the magenta, cyan, and yellow stars in sequence) fusing into the leading front were observed, contributing to the formation of updated and reinforced actin cable (denoted with magenta, cyan, and yellow arrowheads in sequence) over the gap region. The dashed magenta line outlines one follower cell that gradually moved to the leading front (30 min), fused into the leading front (40 min), and finally reinforced the actin-cable segment that formed a prominent purse string over the gap region (50 min; magenta arrowheads). Subsequently, the reinforced purse string at the lead front depolymerized as another follower cell fused into the leading front (80 min; marked with blue manually), which allowed for the recovery of the purse string over the gap (90 min; cyan arrowheads). Finally, the third fusion with actin segment update (yellow star) was observed for the same cell (marked with blue). Scale bar, 10 μm . (C) Color-coded montage of the region of interest (dashed yellow box in B). The dashed white line shows the flow of actin from the follower into the leading front. For A and B, the original time-lapse images without the manually colored marks can be found in [Movies S1, S2, and S3](#).

the lagging of the actin ring behind the advancing gap front (Fig. 3A and *SI Appendix*, Fig. S3, 48 to 66 h), and coexistence of old and new actin-ring segments (e.g., Fig. 3A, 60 h and 66 h), further support the actin-ring segment switching process.

To assess the generality of the mechanism of actin-ring switching and updating, we also examined the monolayer expansion of MDCK cells across nonadhesive gaps (Fig. 4B). Bulk MDCK cells were initially seeded on the adhesive region of the substrate, which was also composed of nonadhesive gaps dotted on the substrate. As the MDCK monolayer encountered and migrated over the nonadhesive gaps, an actin cable was formed, and continued switching of the actin cable among multiple cells was observed (Fig. 4B and *Movie S3*). To better monitor the actin-updating details with the monolayer progression, we captured the actin-time kymograph relative to the gap front (Fig. 4C). The kymograph clearly presents three fusion processes of the actin-ring segments from the follower cells into the leading cells, which allowed for the formation of reinforced actin stress fiber at the front over the gap region. Together, the actin-ring segment switching represents a critical step to shrink the gap size and therefore empowers the purse-string contraction for subsequent gap closure. This presents a gap-closure mechanism in which cell proliferation and migration, large-scale actin-network remodeling, and purse-string contraction are highly coordinated. This mechanism is distinctly different from the classical purse-string contraction mechanism where cell proliferation contributes negligibly to the gap closure and actin fiber fusion/defusion is absent.

Actin Network Remodeling Was Coordinated with Cellular Force Generation and Transmission

Adherent cells exert traction force on the substrate through focal adhesion points. The traction force reacts back onto the cells, driving or resisting gap closure. In a lamellipodial protrusion-based cell crawling mechanism, the traction force on the cells drives gap closure. Thus, the traction force exerting on the substrate measured in the context of the cell crawling mechanism always points outward (so that the reaction force on the cell monolayer points inward). In the present experiments, we hypothesized that the closure of nonadhesive gaps was driven by the actin-ring contraction in a cell proliferation-dependent manner but resisted by the traction force, which acted as a frictional force between the cell monolayer and the hydrogel substrate. To infer the actin-ring contraction, we carried out traction force microscopy (31–33) to measure the traction force landscapes exerted on the hydrogels and monolayer stress microscopy (MSM) (34, 35) to quantify the stress generated in the MDCK monolayer at different stages of the gap-closure process.

Fig. 5 shows the time-lapse traction profiles exerted on the hydrogels by the MDCK monolayers. Taking the radial tractions pointing outward and clockwise-directed tangential tractions as positive, the average radial (\hat{T}_r) and tangential (\hat{T}_θ) traction forces were plotted as a function of the distance from the gap center (r). Note that in the gap region, the traction force is always zero, as cells do not attach to the nonadhesive regions. Vectorial plots of the traction force revealed that cells around the gaps exerted outward radial traction forces onto the hydrogels when cells just became confluent in the adhesive domains (Fig. 5A and B, 40 h), irrespective of the gap size. The outward radial traction is similar to the case in which cells crawl to invade adhesive wounds (36), suggesting that at the beginning of the gap-closure process the cells intended to migrate toward the gap region. Accordingly, the frictional force acting on the cell monolayer was in the inward direction. Note that if the actin-ring contractions were strong enough to pull the monolayer inward, the friction resisting the inward motion would point outward. Thus, the outward radial traction acting on the hydrogel and inward

friction on the cell monolayer suggested that the actin-ring contraction was not strong enough to pull the cell monolayer inward, possibly because the actin ring was just being formed.

After the initial stage, the radial traction switched from an outward to an inward direction; meanwhile, the tangential traction force markedly elevated (Fig. 5A, 48 h, and Fig. 5B, 60 h). The changes of the traction forces along both the radial and tangential directions suggested that the actin ring started to contract strongly. The switch of the cell traction direction was concomitant to the cell attachment onto the edge of the gap. As the attached cells also contract, they may contribute to the inward radial contraction. For a circular gap of 50 μm in radius, the magnitude of the inward radial traction continued to increase while that of the tangential traction force gradually decreased (Fig. 5C, 60 h), correlated with the more concentrated cell distribution along the gap front edge (*SI Appendix*, Fig. S2, 54 h to 66 h). Such a process signified the successful switches of the actin-ring segments and the advance of the gap front. This is because successful actin-ring segment switching effectively shrinks the gap radius, leading to increased radial contraction of the actin ring since the radial contraction is proportional to the local curvature κ . The increasing radial traction in the inward direction and diminishing tangential traction suggested that the actin-ring contraction was sufficiently high to pull the cell sheet inward. Upon the completion of gap closure, the radial traction force remained pointing inward, but its magnitude decreased gradually (Fig. 5A and C, 72 h), suggesting that the cells bridging the gap gradually released residual contractility. This was consistent with the buckling of the cell monolayer arching over the gap at this stage (Fig. 3A, 72 h to 84 h) and the decreasing stress of the bridging cells (*SI Appendix*, Fig. S5). For 100- μm radius gaps, however, the radial cell traction failed to accumulate in an inward direction, while the tangential traction remained on quite a high level (Fig. 5C). This suggested that the actin-ring contraction was not high enough to pull the cell monolayer inward. Eventually, the radial traction switched back to the outward direction (Fig. 5D, 84 h), corresponding to the unsuccessful switching of actin-ring segments and failure of the gap closure.

We carried out MSM (34, 35) to measure the stress landscapes of cell monolayers with 50- and 100- μm radius gaps during the gap-closure process. In MSM, the measured traction force is treated as a body force acting on the cell monolayer due to its thinness, while the actin-ring contraction is imposed as a boundary condition. In a monolayer stress profile, the direction of the first principal stress generally infers the stress fiber orientation, which further suggests the direction and magnitude of cell contractile force generated by actomyosin motors. Taking the first principal stress as σ_1 and its direction as \mathbf{e}_1 , Fig. 6 plots the projections of the first principal stress of the cell monolayer within the region of 20 μm from the advancing gap front onto the radial direction ($\sigma_1 \mathbf{e}_1 \cdot \mathbf{e}_r$), where \mathbf{e}_r denotes the unit vector along the radial direction. The plot showed the radial component of the first principal (RCFP) stress at the initial stage (Fig. 3A and B, 40 h) was small for both gap sizes due to the small contraction at this stage. After the initial stage, the RCFP stress started to increase as the actin ring contracted strongly. For the 50- μm circular gap, the magnitude of average RCFP stress at the gap front increased dramatically from ~ 200 Pa to ~ 500 Pa (Fig. 6A, 48 to 60 h and 50 to ~ 60 μm), corresponding to the increasingly high radial traction and successful gap shrinkage during these time stages. Upon the completion of gap closure, the magnitude of the average RCFP stress at the gap front decreased gradually (Fig. 6A, 60 to 72 h and 50 to ~ 60 μm) as the actin ring released its contractility. For 100- μm -radius gaps, however, the magnitude of average RCFP stress at the gap front only reached about 250 Pa maximum (Fig. 6B, 60 h and 100 to ~ 110 μm), which was insufficient to pull the cells behind the gap front inward. The stress gradually decreased and recovered the initial state

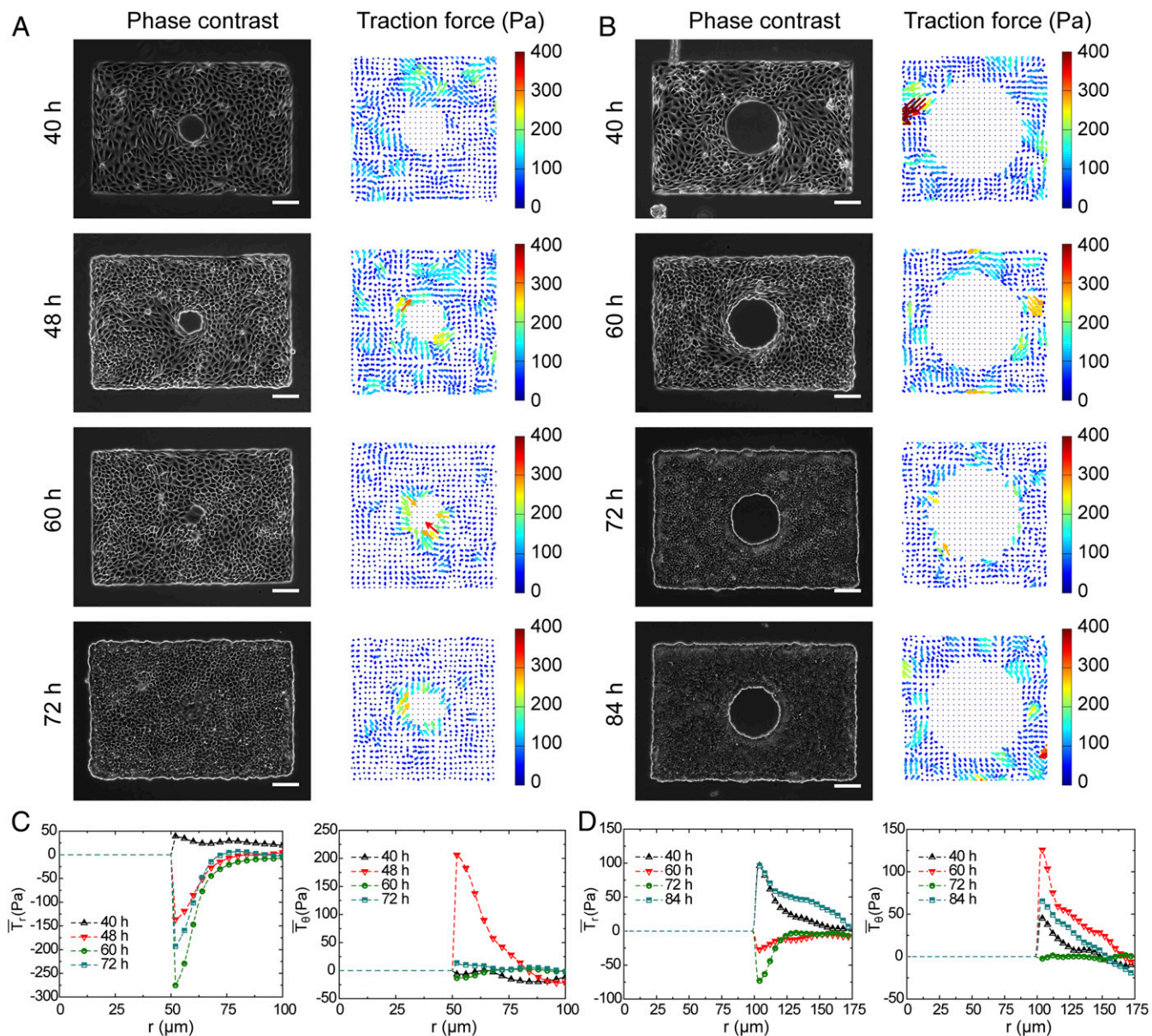


Fig. 5. Traction force microscopy (TFM) of the gap-closure process. (A and B) Phase-contrast images and vector plot of traction force at different gap-closure stages. (A) $R_{eq} = 50 \mu\text{m}$. (B) $R_{eq} = 100 \mu\text{m}$. Scale bar for phase-contrast images, $100 \mu\text{m}$. The size of the traction force maps is $300 \times 300 \mu\text{m}^2$, with the center the same as the initial gap center. (C and D) The average radial and tangential traction forces as a function of distance from the gap center ($r = 0$). (C) $R_{eq} = 50 \mu\text{m}$. (D) $R_{eq} = 100 \mu\text{m}$. TFM was performed on eight parallel samples. Each data point was averaged over $n = 16$ gaps.

(Fig. 6B, 60 to 84 h and 100 to $\sim 110 \mu\text{m}$). As a result, the gap front stayed almost stable from 60 to 84 h (Fig. 3B).

A Kinetic Model for Nonadhesive Gap Closure. We next develop a mechanics-based model to elucidate the curvature-dependent gap-closure kinetics. We first consider a circular actin ring of initial radius R_0 immersed in a viscoelastic medium (the cell monolayer), where the purse-string contraction drives gap closure, while elastic restoring force and viscous drag resist it (SI Appendix, Fig. S6). Neglecting the inertia and elastic-restoring force, the contraction is balanced by the viscous drag: $\eta \frac{\dot{R}}{h} + \kappa\gamma = 0$, where \dot{R} is the rate of change of the radius of the gap (i.e., the actin ring), η is the viscosity of the cell monolayer, and h is the thickness of the actin ring. This follows a simple kinetic evolution for the radius of the actin ring: $\left(\frac{R}{R_0}\right)^2 = 1 - \frac{2\alpha}{R_0^2} t$,

where $\alpha = \gamma h / \eta$. Note that $\beta \equiv \frac{2\alpha}{R_0^2}$ is a rate constant for the gap closure. This kinetic law predicts very well the previous experimental data of gap closure for HaCaT cells (SI Appendix, Fig. S7), where purse-string contraction is the dominant mechanism (16).

For cell proliferation-induced actin-ring segment switching, the radius of the actin ring decreases not only by contraction but also by cell invasion due to the switching. In this case, a modified balance equation arises: $\eta(\dot{R} - \dot{R}_s)/h + \kappa\gamma = 0$, where $-\dot{R}_s$ is the decreasing rate of the radius of the actin ring due to the cell attachment and actin-ring segment switching, which must be excluded from the viscous force. We also assume that the kinetic rate due to actin-ring segment switching is constant, $\dot{R}_s = C$ for $R < R_0$, but vanishes beyond the critical radius, $\dot{R}_s = 0$ for $R \geq R_0$, to account for the curvature-dependent segment switching. This gives rise to a highly nonlinear gap closure kinetics: $R - R_0 + \frac{\alpha}{C} \ln \frac{CR - \alpha}{CR_0 - \alpha} = Ct$.

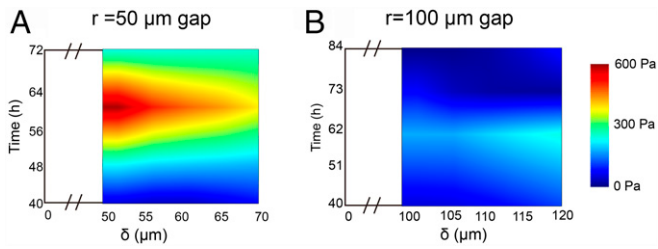


Fig. 6. The change of the radial component of the RCFP stress during the gap closure process as a function of distance from the gap center ($r = 0$). (A) The change of RCFP for the 50- μm -radius gap. (B) The change of RCFP for the 100- μm -radius gap.

Overall, this solution captures the closure kinetics of small circular gaps observed in the experiments (Fig. 7A).

For elliptical gaps, the closure kinetics varies at the different positions at the gap front, owing to the curvature-dependent actin-ring segment switching. Accordingly, the balance equation is modified to $\eta(\dot{\mathbf{x}} - \dot{\mathbf{x}}_s)/h + \kappa\gamma\mathbf{n} = 0$, where \mathbf{x} is the position vector at the gap front; $-\dot{\mathbf{x}}_s$ is the rate of change of the position of the actin ring due to the cell attachment and actin-ring segment switching, which is assumed to be a constant here; and \mathbf{n} is the outer unit normal of the gap front. The kinetic equation can be solved numerically to track the gap front, as shown in Fig. 7A and B. Our simulation captures the morphological changes of elliptical gaps, that is, from an ellipse to a circle (Fig. 7B).

Discussion

Cells employ different mechanisms to close physical gaps, depending on the gap properties. For adhesive gaps, lamellipodial protrusion-based cell crawling generates outward traction onto the ECM, corresponding to an inward pulling force on the cells that drives gap closure (6, 22), a scenario resembling human walking. For nonadhesive gaps, purse-string contraction is the central driving force, and the long-range cell-ECM interactions generate outward friction onto the cells that resists gap closure (16). Corresponding to the limit of the cell's contractile machinery, there exists a gap-size limit beyond which the actin-ring contraction is insufficient to overcome the resistant force and gap closure fails to complete. Such contractility-limited gap size dependence has been widely adopted to elucidate the closure behavior of nonadhesive gaps (16, 19).

Cells may invoke additional mechanisms to break the size limit in purse-string contraction-enabled gap closure. In a recent 3D biomimetic model, Sakar et al. (28) revealed that tangentially migrating fibroblasts along the wound edge can tow and assemble a fibronectin template inside the gap, thereby actively modify the surface properties of the gap regions and facilitate cells to complete closure. Nier et al. reported that in addition to purse-string contraction, active epithelial fluctuation at the gap front plays an essential role in nonadhesive gap closure (19). Yet, the structural basis of the active fluctuation was unclear. The numerical model based on the fluctuation force concluded that an arbitrarily large gap could close if sufficiently long cell culture time was given. In all of the previous studies, cell proliferation either did not play a role in the gap closure (16, 28) or was not examined (19) despite the speculation that proliferative pressure may be essential to nonadhesive gap closure (16). Here, we have shown that the closure of the nonadhesive gaps by MDCK cells can be assisted by cell-proliferative pressure, collective cell migration, and subsequent large-scale, intercellular actin remodeling at the gap front, which is distinctly different from the classical purse-string contraction or lamellipodia-dependent cell crawling. Our experimental studies reveal that the actin-ring segment switching necessitates cell proliferation and curvature-

dependent actin-network fusion and remodeling, rendering the nonadhesive gap closure a proliferation-limiting, size-dependent process.

The size-dependent gap-closure behavior may be attributed to the curvature-sensing ability of cells (17, 18). As a migrating cell encounters a concave curvature, an actin flow is directed toward the cell front, promoting the formation of a contractile actin cable that enables cells bridging over nonadhesive gaps. In contrast, when a cell encounters a convex curvature, a retrograde actin flow is generated at the convex edges, leading to the formation of lamellipodial protrusions that facilitate cell crawling on adhesive substrates. Such curvature sensing and adaption must have occurred in our experiments. As a cell migrates and attaches onto the actin ring at the gap front, it senses the local curvature and generates an actin-ring segment. Owing to the presence of the newly attached cells, the old cell becomes distanced from the curvature and its actin-ring segment dissociates, reflecting a negative feedback. Thus, the actin-ring segment switching occurs, and the newly attached cell joins the tug-of-war team to form a complete actin ring. Evidently, the curvature-sensing ability of cells is dependent on curvature. Large concave curvatures (small gaps) may generate stronger anterograde actin flow (17, 18), resulting in a stronger actin-ring segment in the newly attached cells, which facilitates the fusion and switching process. However, for small concave curvatures or for convex curvatures, such actin-ring segment switching fails, and the gap-closure process ceases. More detailed experimental evidence is required to further validate the curved-dependent actin dynamics in the nonadhesive gap closure.

In summary, we have shown that nonadhesive gap closure by MDCK cells is coordinated by cell proliferation, actin-network remodeling, and purse-string contraction. Proliferative pressure pushes cells to attach onto the gap front, causing large-scale actin remodeling. The consecutive actin-ring segment switching narrows the gap and increases the curvature, and hence it empowers the actin-ring contraction and facilitates subsequent gap closure. Successful actin-ring segment switching is signified by the persistent rise of the radial components of the traction force and monolayer stress, manifesting the close reciprocity between mechanics, cellular structure modeling, and biochemistry in the gap-closure process. Our data offer fundamental insights into a previously unexplored mechanism in closure of nonadhesive gaps and may stimulate new efforts to examine possible *in vivo* counterparts.

Materials and Methods

Live-Cell Imaging. Stable MDCK cells expressing LifeAct-GFP were prepared based on the manufacturer's protocol (iBidi, rLV-Ubi-LifeAct). Cells were then incubated with selection antibody puromycin at 1.5 $\mu\text{g}/\text{mL}$ for 7 d and were further selected with fluorescence-activated cell sorting (Beckman

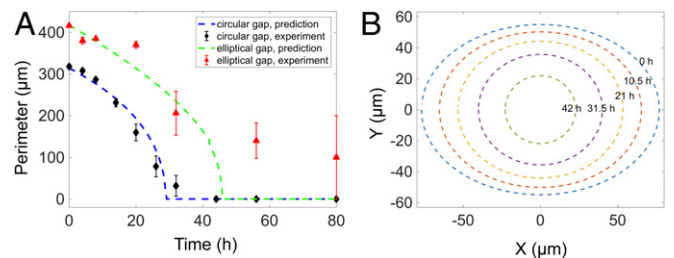


Fig. 7. Modeling of the gap closure kinetics. (A) A model prediction of the gap perimeter changes with time in comparison with experimental data ($n = 5$ for the elliptical gap; $n = 13$ for the circular gap). The experimental data are from three parallel experiments. (B) The predicted morphological change of an elliptical gap with a semimajor axis of 75 μm and a semiminor axis of 50 μm at different time points.

Coulter's MoFlo Astrios EQ) to remove the untransfected cells. In live imaging, the dynamics of wound closure were monitored by taking time-lapse wound images every 30 min.

For cell invasion assay on dotted substrate, MDCK cells tagged with LifeAct-RFP (Red Fluorescent Protein) were seeded at the density of 50,000 cell/cm² and cultured for 24 h. Upon reaching 100% confluency, the polydimethylsiloxane stencil was removed to initiate the epithelial migration, and fresh medium was refilled. The process of epithelial migration over nonadhesive circle arrays were then imaged on a confocal laser scanning microscope (Leica DMI8) at the interval of 5 min for over 3 h.

Traction Force Microscopy. Fluorescent beads (200 nm in diameter, Life Technologies) embedded on the subsurface of PAA gel were used as the tracer of gel deformation. A pair of fluorescent images of beads taken before and after detaching MDCK cells from the gel were collected at different closure stages. The in-plane displacement field and the traction force were extracted as previously described (31, 32).

Data Analysis and Statistics. The closure probability was calculated as the number of closed gaps on day 5 over the total number of gaps with that given size under each experimental condition. The statistical analysis was performed in OriginPro 8.0 using a Student's two-tailed *t* test. Data are presented as mean \pm SEM. A value of *P* > 0.05 is considered as no statistically significant difference. All experiments were repeated three times unless otherwise stated, and statistical analysis was based on data from the parallel experiments.

Data Availability. All study data are included in the article text and supporting information.

ACKNOWLEDGMENTS. S.Z. acknowledges support by the NIH (National Heart, Lung, and Blood Institute R21-HL122902) and NSF (Civil, Mechanical and Manufacturing Innovation-0754463/0644599). J.Y. was supported in part by National Institute of Arthritis and Musculoskeletal and Skin Diseases Award (AR072731).

1. P. Martin, Wound healing—Aiming for perfect skin regeneration. *Science* **276**, 75–81 (1997).
2. A. Jacinto *et al.*, Dynamic actin-based epithelial adhesion and cell matching during *Drosophila* dorsal closure. *Curr. Biol.* **10**, 1420–1426 (2000).
3. D. P. Kiehart, C. G. Galbraith, K. A. Edwards, W. L. Rickoll, R. A. Montague, Multiple forces contribute to cell sheet morphogenesis for dorsal closure in *Drosophila*. *J. Cell Biol.* **149**, 471–490 (2000).
4. W. Wood *et al.*, Wound healing recapitulates morphogenesis in *Drosophila* embryos. *Nat. Cell Biol.* **4**, 907–912 (2002).
5. W. M. Bement, C. A. Mandato, M. N. Kirsch, Wound-induced assembly and closure of an actomyosin purse string in *Xenopus* oocytes. *Curr. Biol.* **9**, 579–587 (1999).
6. A. Brugués *et al.*, Forces driving epithelial wound healing. *Nat. Phys.* **10**, 683–690 (2014).
7. A. Jacinto, A. Martinez-Arias, P. Martin, Mechanisms of epithelial fusion and repair. *Nat. Cell Biol.* **3**, E117–E123 (2001).
8. C. D. Nobes, A. Hall, Rho GTPases control polarity, protrusion, and adhesion during cell movement. *J. Cell Biol.* **144**, 1235–1244 (1999).
9. G. Fenteany, P. A. Janmey, T. P. Stossel, Signaling pathways and cell mechanics involved in wound closure by epithelial cell sheets. *Curr. Biol.* **10**, 831–838 (2000).
10. A. J. Copp, F. A. Brook, J. P. Estibeiro, A. S. Shum, D. L. Cockcroft, The embryonic development of mammalian neural tube defects. *Prog. Neurobiol.* **35**, 363–403 (1990).
11. J. H. Miner, J. Cunningham, J. R. Sanes, Roles for laminin in embryogenesis: Encephaly, syndactyly, and placentopathy in mice lacking the laminin α 5 chain. *J. Cell Biol.* **143**, 1713–1723 (1998).
12. Y. Danjo, I. K. Gipson, Actin 'purse string' filaments are anchored by E-cadherin-mediated adherens junctions at the leading edge of the epithelial wound, providing coordinated cell movement. *J. Cell Sci.* **111**, 3323–3332 (1998).
13. P. Martin, J. Lewis, Actin cables and epidermal movement in embryonic wound healing. *Nature* **360**, 179–183 (1992).
14. J. M. Russo *et al.*, Distinct temporal-spatial roles for rho kinase and myosin light chain kinase in epithelial purse-string wound closure. *Gastroenterology* **128**, 987–1001 (2005).
15. M. Tamada, T. D. Perez, W. J. Nelson, M. P. Sheetz, Two distinct modes of myosin assembly and dynamics during epithelial wound closure. *J. Cell Biol.* **176**, 27–33 (2007).
16. S. R. K. Vedula *et al.*, Mechanics of epithelial closure over non-adherent environments. *Nat. Commun.* **6**, 6111 (2015).
17. T. Chen *et al.*, Large-scale curvature sensing by directional actin flow drives cellular migration mode switching. *Nat. Phys.* **15**, 393–402 (2019).
18. S. R. K. Vedula *et al.*, Epithelial bridges maintain tissue integrity during collective cell migration. *Nat. Mater.* **13**, 87–96 (2014).
19. V. Nier *et al.*, Tissue fusion over nonadhering surfaces. *Proc. Natl. Acad. Sci. U.S.A.* **112**, 9546–9551 (2015).
20. M. Deforet, V. Hakim, H. G. Yevick, G. Duclos, P. Silberzan, Emergence of collective modes and tri-dimensional structures from epithelial confinement. *Nat. Commun.* **5**, 3747 (2014).
21. Q. Tseng *et al.*, A new micropatterning method of soft substrates reveals that different tumorigenic signals can promote or reduce cell contraction levels. *Lab Chip* **11**, 2231–2240 (2011).
22. E. Anon *et al.*, Cell crawling mediates collective cell migration to close undamaged epithelial gaps. *Proc. Natl. Acad. Sci. U.S.A.* **109**, 10891–10896 (2012).
23. J. V. Moyano, P. G. Greciano, M. M. Buschmann, M. Koch, K. S. Matlin, Autocrine transforming growth factor-beta1 activation mediated by integrin alphaVbeta3 regulates transcriptional expression of laminin-332 in Madin-Darby canine kidney epithelial cells. *Mol. Biol. Cell* **21**, 3654–3668 (2010).
24. V. Iorio, L. D. Troughton, K. J. Hamill, Laminins: Roles and utility in wound repair. *Adv. Wound Care (New Rochelle)* **4**, 250–263 (2015).
25. G. Z. Mak *et al.*, Regulated synthesis and functions of laminin 5 in polarized madin-darby canine kidney epithelial cells. *Mol. Biol. Cell* **17**, 3664–3677 (2006).
26. D. E. Discher, P. Janmey, Y. L. Wang, Tissue cells feel and respond to the stiffness of their substrate. *Science* **310**, 1139–1143 (2005).
27. R. G. Wells, The role of matrix stiffness in regulating cell behavior. *Hepatology* **47**, 1394–1400 (2008).
28. M. S. Sakar *et al.*, Cellular forces and matrix assembly coordinate fibrous tissue repair. *Nat. Commun.* **7**, 11036 (2016).
29. J. Brock, K. Midwinter, J. Lewis, P. Martin, Healing of incisional wounds in the embryonic chick wing bud: Characterization of the actin purse-string and demonstration of a requirement for Rho activation. *J. Cell Biol.* **135**, 1097–1107 (1996).
30. W. M. Bement, P. Forscher, M. S. Mooseker, A novel cytoskeletal structure involved in purse string wound closure and cell polarity maintenance. *J. Cell Biol.* **121**, 565–578 (1993).
31. Q. Tseng *et al.*, Spatial organization of the extracellular matrix regulates cell-cell junction positioning. *Proc. Natl. Acad. Sci. U.S.A.* **109**, 1506–1511 (2012).
32. B. Sabass, M. L. Gardel, C. M. Waterman, U. S. Schwarz, High resolution traction force microscopy based on experimental and computational advances. *Biophys. J.* **94**, 207–220 (2008).
33. J. P. Butler, I. M. Tolić-Nørrelykke, B. Fabry, J. J. Fredberg, Traction fields, moments, and strain energy that cells exert on their surroundings. *Am. J. Physiol. Cell Physiol.* **282**, C595–C605 (2002).
34. D. T. Tambe *et al.*, Collective cell guidance by cooperative intercellular forces. *Nat. Mater.* **10**, 469–475 (2011).
35. D. T. Tambe *et al.*, Monolayer stress microscopy: Limitations, artifacts, and accuracy of recovered intercellular stresses. *PLoS One* **8**, e55172 (2013).
36. X. Trepap *et al.*, Physical forces during collective cell migration. *Nat. Phys.* **5**, 426–430 (2009).